



1 *Conference Proceedings Paper*

2 **Antarctic sea ice extent from ISRO's SCATSAT-1** 3 **using PCA and an unsupervised classification**

4 **Rajkumar Kamaljit Singh¹, Khoisnam Nanaoba Singh¹, Mamata Maisnam¹, and Jayaprasad P²**

5 ¹ National Institute of Technology Manipur, Imphal, India

6 ² Space Applications Centre-ISRO, Ahmedabad, India

7 Published: date

8 **Abstract:** Indian Space Research Organisation's SCATSAT-1 is a continuity mission for Oceansat-2
9 Scatterometer. The sensor works in Ku-band (13.515 GHz) similar to the one flown on-board
10 Oceansat-2. It provides backscattering coefficient over the globe and wind vector data products over
11 the oceans that are useful for weather forecasting, cyclone detection and tracking services. Besides
12 backscattering coefficient (sigma nought), two other important parameters namely, Gamma nought
13 (obtained from backscattering coefficient) and Brightness temperature (obtained from scatterometer
14 noise measurement) are given as the Level-4 data products archived at the ISRO's Meteorological &
15 Oceanographic Satellite Data Archival Centre. We used these three parameters both in horizontal
16 and vertical polarizations for the Antarctic region (South Polar) to perform, first, a principal
17 component analysis. Then, we used the first three principal components explaining the largest
18 variability in the data set to perform an unsupervised ISODATA clustering classification to estimate
19 the regions of sea ice around Antarctica. The derived sea ice extent through this method is compared
20 with other popular sea ice extent products available elsewhere.

21 **Keywords:** SCATSAT-1; Antarctic sea ice extent; principal component analysis; ISODATA
22 classification
23

24 **1. Introduction**

25 With an extreme variability of about 20 Million km² (during austral winter) to about 3 Million
26 km² (austral summer) (Comiso, 2003; Gloersen et al., 1992), Antarctic sea ice plays as a sensitive
27 indicator of climate change and a modulator of the global climate system (Lubin and Massom, 2006).

28 Formation of sea ice in autumn from saline ocean water is associated with heat losses and a
29 change in salinity fluxes, which help in formation of Antarctic Deep and Bottom water (Lubin and
30 Massom, 2006). It is the driver of global thermohaline circulation. Moreover, during melt season, the
31 melting sea ice introduces a layer of fresh-water which helps in stabilizing mixed layer and also in
32 decreasing its depth (Timmermann et al., 2001), thereby, moderating deep ocean convection
33 stabilizing large-scale global ocean thermohaline circulation patterns (Aagard and Carmack, 1989;
34 Martinson and Iannuzzi, 1998).

35 A microwave sensor has little sensitivity to cloud cover and it is not affected by day-night
36 change. Because of these properties, use of microwave sensors (both active (e.g., scatterometer etc.)
37 as well as passive (e.g., radiometer) for observing Polar Regions is the most convenient form of
38 satellite-based remote sensing of these regions. Antarctic sea ice cover has been derived using both
39 active (Remund and Long, 1999, 2014, etc.) and passive sensors (Cavalieri et al., 1997; Comiso, 2003,
40 etc.).

41 In this study, we have used the multivariate technique Principal Component Analysis (PCA)
42 and K-means (ISODATA) classification on the enhanced resolution Level-4 data from the recently

43 launched Indian Space Research Organisation's SCATSAT-1 to derive sea ice extent (SIE) around
44 Antarctica for the period 2016-17. The derived extents are then compared with passive microwave
45 derived sea ice extents and with SAR data for some regions around Antarctica.

46 The paper has been arranged in the following manner. Section 2 presents the data used in the
47 study, while Section 3 gives details about the methodology employed and the generation of SIE from
48 SCATSAT-1. Results and discussions including the comparisons with passive microwave and SAR
49 data are given in Section 4. The paper is then concluded with some remarks and possible future scope
50 in Section 5.

51 2. Datasets

52 SCATSAT-1, launched in September, 2016, is a mini-satellite carrying a Ku-band (13.515 GHz)
53 scatterometer, same as that was in Oceansat-2. It is a conically scanning, dual-pencil beam
54 scatterometer with the outer beam vertically polarized and the inner, horizontally polarized. The
55 instrument was developed primarily to provide wind data for weather forecast and cyclone
56 detection. However, it has applications over the Polar Regions for ice studies.

57 Even though the highest nominal resolution of the wind vector cell is 25 km (ISRO, 2018), Level-
58 4 data products have spatial resolutions as high as ~2 km. There are altogether six Level-4 data
59 products generated at the moment. The datasets used in this study is the SouthPolar24 both in vertical
60 and horizontal polarization. This dataset is generated from Level-1B data using both ascending and
61 descending passes of the backscattering coefficient (σ_0) and other radiometric parameters for
62 the past 24-hr (more details about the product in the manual of SCATSAT1 DP Team, 2017). The
63 parameters containing in this Level-4 data are σ_0 (σ_0), γ_0 (γ_0) and brightness
64 temperature (T_b). The dataset is archived at the ISRO's data archival centre, Meteorological &
65 Oceanographic Satellite Data Archival Centre, MOSDAC (<https://mosdac.gov.in/>).

66 The derived sea ice extents (SIE) are compared with the extents obtained from passive
67 microwave observations. Advanced microwave scanning radiometer-2 (AMSR2) on-board the Japan
68 Aerospace Exploration Agency- JAXA's Global Change Observation Mission-Water (GCOM-W or
69 "Shizuku") satellite constantly observes the sea ice regions of the Earth. Remote Sensing of Polar
70 Regions research group at the Institute of Environment Physics (IUP), University of Bremen,
71 generates sea ice concentration (SIC) data for both the Polar Regions. The SIC data are derived at
72 3.125 km and 6.25 km resolution respectively using the ARTIST Sea Ice algorithm (Spren, et al., 2008)
73 and the Bootstrap algorithm (Comiso, 1995). We use 15% SIC in both the data products as the
74 threshold to designate a pixel as sea ice [Zwally et al., 1983; Comiso and Nishio, 2008] and generate
75 sea ice extent maps using this threshold.

76 The third dataset that we have used here is the Sentinel-1A/1B SAR Level-1 Extra Wide (EW)
77 Ground Range Detected (GRD) swath imageries at medium resolution ~93×87 m (ESA Sentinel User
78 Guide, 2018). The imageries are downloaded from the Polar View data archival website
79 (www.polarview.org). Polar View is an international consortium of sea ice experts from nine
80 countries across Europe and Canada, providing near real-time sea ice information.

81 Moreover, ice chart shapefiles from the U.S. National Ice Center/Naval Ice Center
82 (www.natice.noaa.gov/Main_Products.htm) are also downloaded for a few days to compare with our
83 SCATSAT-1 sea ice maps.

84 To remove ambiguous sea ice signatures coming at the locations where historically sea ice is
85 never expected to exist, we have created a maximum boundary beyond which sea ice detection is not
86 carried out. This mask is created using the Southern Hemisphere sea ice occurrence probability
87 (SIOP) dataset (Rajak et al., 2015) archived at the MOSDAC. This dataset is produced using passive
88 microwave daily-averaged sea ice concentration data from 1978 through 2012. We define the
89 maximum sea ice boundary using those pixels which have been classified as sea ice at least 3 times
90 in the given period of 35 years (3.5 years correspond to a probability value of 10 for this given dataset).
91 This mask, which is in essence the climatologically maximum Antarctic sea ice edge, is applied to all
92 the sea ice maps generated from all the three source datasets viz., SCATSAT-1, ASI and BT.

93 3. Methodology

94 3.1. Principal component analysis

95 It has been shown by Rothrock and Thomas (1988) and Piwowar and LeDrew (1996), etc. that
96 the technique of PCA can be extensively used to study sea ice in the Arctic. Moreover, Lillesand et al.
97 (2016) described the usefulness of PCA in analysing remotely sensed imagery.

98 PCA is a very popular multivariate statistical technique. It is traditionally used as a dimension
99 reduction tool to reduce from a large set of variables to a small set. Its main feature is to extract
100 important information about the given data sample and represent a set of new orthogonal variables,
101 called principal components (Abdi and Williams, 2010). In case of multiband remote sensing data,
102 this analysis helps in identifying distinct spatial and spectral patterns (Piwowar and LeDrew, 1996).

103 In this study, we perform PCA over the three scatterometer parameters mentioned above in both
104 horizontal and vertical polarizations. Therefore, there are altogether 6 parameters (3 parameters×2
105 polarizations). Six different regions around Antarctica where different features of ice/ocean classes
106 are expected to exist, are selected (Fig. 1). Ten dates chosen for PCA are 1 December, 2016, 14
107 December, 2016, 30 December, 2016, 1 February, 2017, 15 February, 2017, 28 February, 2017, 2 May,
108 2017, 16 May, 2017, 30 May, 2017 and 7 October, 2017. There are 240000 usable data points per
109 parameter per day from all the six regions. Using Minitab, PC coefficients are generated from the six
110 input parameters (Table 1) and the Scree plot is given in Fig. 2. Using these coefficients, we generate
111 the required Principal Components. Even though, the Scree plot suggests that only two components
112 are good enough to explain maximum variability of the given data sample, we have retained three
113 components in this analysis so that we can generate an RGB image.

114 A sample of the generated principal components for a particular day is given in Fig. 3 top panel
115 (a-c). The first principal component (PC1) explains the largest percentage of total variance (Lillesand
116 et al., 2016) followed by PC2 and PC3. The false-colour composite (FCC) image, shown at the bottom
117 of Fig. 3c, is generated using these three principal components as the input channels of red, green
118 and blue respectively. In this FCC, regions with pinkish and greyish shades represent the sea ice area
119 around Antarctica while the green and black shades represent ocean. The FCC RGB image is
120 transformed to hue, saturation, value (HSV) colour space (Fig. 3d) using the HSV transformation in
121 ENVI software. This process replaces the value band with the high-resolution image, then it
122 automatically resamples the hue and saturation bands to the high-resolution pixel size using cubic
123 convolution technique. And ultimately, there is the final transformation of the image back to RGB
124 colour space. The output RGB images will have the pixel size of the input high-resolution data.
125 Subsection

126 3.2. Unsupervised classification of image:

127 Next step is to segregate this sea ice region from the ocean pixels. To achieve this, we perform
128 an unsupervised image classification because there are no a priori training data to classify sea
129 ice/ocean pixels. An unsupervised classifier does not require training data and the classification is
130 achieved by aggregating unknown pixels into different classes through natural grouping or
131 clustering. The basic idea is that pixels belonging to a specific feature type should have nearby values
132 in the measurement space compared to those pixels of different classes which should be well
133 separated (Lillesand et al., 2016).

134 Here, we have used the multivariate statistical analysis technique in ArcGIS, known as the Iso-
135 cluster unsupervised classification using the HSV sharpened image described above. This technique
136 is based on the Iterative Self-Organizing Data Analysis Technique (ISODATA) (Tou and Gonzalez,
137 1974; Lillesand et al., 2016) algorithm of k-means clustering and additionally, maximum likelihood
138 classification. In addition to this, a generalization analysis technique (Majority filter) that replaces
139 cells in a raster based on the majority of their contiguous neighbouring cells. This helps in cleaning
140 up of small erroneous data in the raster. Finally, sea ice boundary mask for the particular day, is then
141 applied, thereby, reducing the ambiguous signals in regions where sea ice is not expected to exist.

142 The sea ice map for 3 December, 2016, determined from SCATSAT-1 is shown in Fig. 4. The blue
143 solid line is the sea ice boundary estimated from passive microwave data obtained by identifying
144 pixels having more than 15% sea ice concentration. The formation of polynyas at different places
145 around Antarctica is very well picked up by the method described here. This feature will be used in
146 future for studying Antarctica polynya dynamics, particularly, the Weddell Sea polynya. Detailed
147 discussion on the comparison is given in the next section.

148 4. Comparison with passive microwave and SAR data

149 4.1. Passive microwave data

150 For the purpose of comparison, the sea ice products viz., SCATSAT-1, ASI and BT sea ice maps
151 are projected into South Polar stereographic 6.25 km spatial resolution (BT's resolution- the coarsest
152 of the three) using the layer stacking tool in ENVI.

153 Forty eight dates from six different months (a few days in the beginning, middle and the end of
154 each month) corresponding to one complete life-cycle of sea ice in the Antarctic oceans are chosen for
155 comparative analysis. The sea ice extents derived from the above mentioned three methods for these
156 48 days are shown in Fig. 5. The root mean squared error for (i) SCATSAT-1 Vs Bootstrap and (ii)
157 SCATSAT-1 Vs ASI are ~0.4 Million Sq. km in both the cases. Moreover, there is a high degree of
158 correlation ($r = 0.99$) between the sea ice extents in both the comparisons.

159 In order to test the statistical significance of the results, we performed first the Fisher's F-test
160 (Table 2) to check the variance between the pair of datasets (SC1 Vs BT and SC1 Vs ASI). Since the
161 calculated F-value is smaller than the critical F-value, we accept the null hypothesis that the datasets
162 have statistically equal variance. This test acts as a precursor for the next statistical test, the Student's
163 t-test to check the differences in population means of these datasets. We perform two sample, two-
164 tail t-test for comparing (a) SCATSAT-1(SC1) Versus Bootstrap (BT) and (b) SC1 Versus ASI. The t-
165 test statistics are given in Table 3 for both the cases. Absolute values of the calculated statistic ('t stat',
166 in the tables) are smaller than the standard critical values for two-tail test ('t Critical two-tail'). Hence,
167 we cannot reject the null hypothesis that is, the population means do not differ significantly. It may
168 be noted here that all the statistical tests are done at 95% confidence level. Moreover, p-values are
169 larger than 0.05 (the predefined significant level, alpha for the statistical tests).

170 To further introspect into the matter, we perform a pixel-wise accuracy mapping between the
171 estimated SCATSAT-1 SIE and the other two estimates (Fig. 6). We map each pixel classified as either
172 ocean or sea ice in the Bootstrap or ASI imagery against the pixel in the SCATSAT-1 imagery after re-
173 projecting them into one common projection with a spatial resolution of 6.25 km. In the figure, 'Oc'
174 represents ocean and 'Ic', sea ice. Hence, SC1_Oc:BT_Oc represents the mapping accuracy for
175 classifying pixels classified as ocean in Bootstrap algorithm as ocean in SCATSAT-1 estimation.
176 Similarly, SC1_Ic:BT_Ic represents the sea ice classification accuracy in both the estimates. Number
177 of pixels taken for comparison on each day is also plotted denoted by the 'crosses'. There is an overall
178 ice-to-ice mapping accuracy of 96% in SC1-BT and ~99% in SC1-ASI comparison. As shown in the
179 plots, there are, however, some misclassifications as well (e.g., SC1_Oc:BT_Ic). Nonetheless, they are
180 only ~10% or less in most of the cases.

181 4.2. SAR data

182 We process the Sentinel-1 EW GRD data in the Sentinel Application Platform or SNAP. The
183 detailed process is as follows:

- 184 1) Creation of a calibration look-up table for conversion of DN values to σ_0 ,
- 185 2) Radiometric correction for removal of noise 3) speckle filtering using Lee-sigma filter,
- 186 3) Radiometric calibration to convert DN values to the corresponding σ_0 using the look-up table,
187 and
- 188 4) Geometric correction (ellipsoid correction) and re-projection to NSIDC South polar
189 stereographic.

190 For this study, we have chosen three sites in East Antarctica (Fig. 7). The white solid line is the
191 sea ice edge estimated by our SCATSAT-1 algorithm for 20 January, 2018. It is apparent our sea ice
192 edge is closely matching the SAR imagery. However, it may be noted here that the SAR scenes are
193 one-minute observation of the region at a given local time and our SCATSAT-1 data are daily-
194 averaged. Therefore, there will be some differences in the observation even though the “actual” sea
195 ice edge looks similar to our estimated edge.

196 4.3. Ice chart shapefiles

197 To complete the comparative analysis, we check the effectiveness of SCATSAT-1 sea ice
198 algorithm in comparison to the ice edge obtained from an operational ice chart (Fig. 8). We have
199 compared the results for a few days but shown here the comparison for 20 January, 2018.

200 The US NIC ice edge chart identifies the sea ice pack shown in red as those pixels having 8-
201 10/10ths or greater of sea ice, while the Marginal Ice Zone (MIZ) where there are lesser concentration
202 of sea ice are shown in yellow. MIZ are the regions where ambiguities in the detection of sea ice edge
203 using satellite remote sensing data can occur. This is due to the mixing of electromagnetic signatures
204 returning from both sea ice and open ocean and the errors can be even larger during summer melting
205 season of sea ice (Comiso and Nishio, 2008).

206 It is apparent from this analysis that our SCATSAT-1 sea ice edge is in close match with the sea
207 ice pack region as identified in the ice chart. We may notice distinctly that the Ross Sea polynya is
208 clearly identified in our sea ice detection algorithm as it is in the ice chart.

209 5. Conclusion

210 We made an attempt to develop an algorithm for the detection of sea ice in the Southern Oceans
211 and to estimate the austral sea ice extent. The algorithm used the Indian Space Research
212 Organisation’s SCATSAT-1 enhanced resolution data from the first year of operation at a spatial
213 resolution of 2.225 km.

214 The algorithm used a combination of techniques such as the Principal Component Analysis and
215 image classification technique (ISODATA k-means classifier). The sea ice estimates (edge and extent)
216 from this method are found to have a high degree of correlation with other available high quality sea
217 ice products. Pixel-wise accuracy mapping reveals there is an overall ice-to-ice mapping accuracy of
218 about 99% when compared with ARTIST Sea Ice (ASI)-derived sea ice extent and 96% when
219 compared with Bootstrap. Ocean-to-ocean mapping accuracy is also high (in excess of 90%).

220 Moreover, in comparison with high resolution SAR and ice chart data, the algorithm tends to
221 perform satisfactorily.

222 In future, the algorithm will be applied for the detection of important Antarctic polynyas such
223 as those occurring in Weddell Sea and Ross Sea, to study their dynamics. **Acknowledgments:** All
224 sources of funding of the study should be disclosed. Please clearly indicate grants that you have
225 received in support of your research work. Clearly state if you received funds for covering the costs
226 to publish in open access.

227 **Author Contributions:** This work is funded by the collaborative ISRO-NIT Manipur science project, “Signature
228 analysis, monitoring ice calving events and marginal changes using SCATSAT-1 data over Antarctica”. The
229 authors, Rajkumar Kamaljit Singh, Khoisnam Nanaoba Singh and Mamata Maisnam, thank the Space
230 Applications Centre-ISRO, India for this project. Special acknowledgement goes to Mr. Shashikant Patel, former
231 JRF SAC-ISRO, for his help on using ArcGIS.

232 **Conflicts of Interest:** The authors declare no conflict of interest.

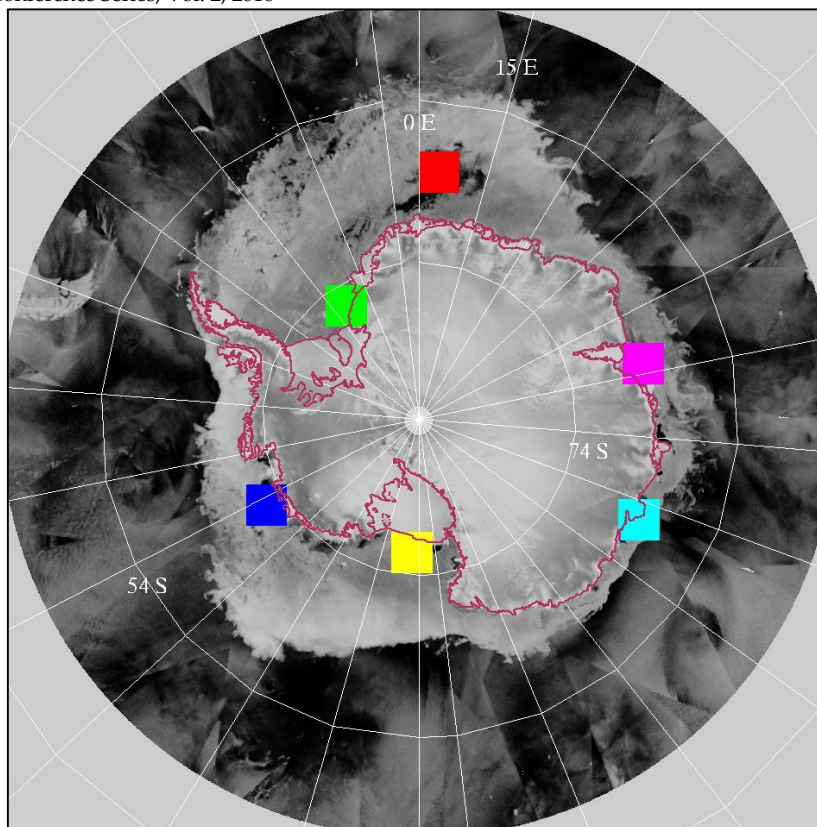
233 References

- 234 1. Aagard, K. and E.C. Carmack, 1989: The role of sea ice and other fresh water in the Arctic circulation,
235 Journal of Geophysical Research, 94(C10), pp. 14485–14498.

- 236 2. Abdi, H., and L.J. Williams, 2010: Principal component analysis, Wiley Interdisciplinary Reviews:
237 Computational Statistics, pp. 433-459, DOI: 10.1002/wics.101.
- 238 3. Cavalieri, D. J., P. Gloersen, C. L. Parkinson, , J. C. Comiso, and H. J. Zwally, 1997: Observed hemispheric
239 asymmetry in global sea ice changes. *Science*, 278, pp. 1104–1106
- 240 4. Comiso, J.C., 1995: SSM/I Concentrations Using the Bootstrap Algorithm, NASA Reference Publication
241 1380.
- 242 5. Comiso, J.C., 2003: Large-scale characteristics and variability of the global sea ice cover. In: D. Thomas and
243 G. Dieckmann (eds.), *Sea ice: An introduction to its physics, chemistry, biology and geology*, Blackwell
244 Scientific, Oxford, UK, pp. 112–142.
- 245 6. Comiso, J.C., and F. Nishio, 2008: “Trends in the sea ice cover using enhanced and compatible AMSR-E,
246 SSM/I, and SMMR data”, *Journal of Geophysical Research*, Vol-113 (C02S07), doi:10.1029/2007JC004257.
- 247 7. Comiso, J.C., and F. Nishio, 2008: Trends in the sea ice cover using enhanced and compatible AMSR-E,
248 SSM/I, and SMMR data, *Journal of Geophysical Research*, Vol. 113(C02S07), doi:10.1029/2007JC004257.
- 249 8. ESA Sentinel User Guide, 2018: [https://sentinel.esa.int/web/sentinel/user-guides/sentinel-1-
250 sar/resolutions/level-1-ground-range-detected](https://sentinel.esa.int/web/sentinel/user-guides/sentinel-1-sar/resolutions/level-1-ground-range-detected) (Online. Accessed on January, 2018)
- 251 9. Gloersen, P.; W.J. Campbell; D.J. Cavalieri; J.G. Comiso; C.L. Parkinson and H.J. Zwally, 1992: Arctic and
252 Antarctic sea ice, 1978-1987: Satellite passive-microwave observations and analysis (NASA special
253 publication SP-511), NASA Goddard Space Flight Center, Greenbelt, MD, pp 290
- 254 10. ISRO, 2018: “SCATSAT-1 Wind Products (BETA Version) Released”, [https://www.isro.gov.in/SCATSAT-
255 1-wind-products-beta-version-released](https://www.isro.gov.in/SCATSAT-1-wind-products-beta-version-released). Online. Accessed on 22 Jan. 18
- 256 11. Lillesand, T.M., R.W. Kiefer, and J.W. Chipman, 2016 (eds.), 1987: *Remote Sensing and Image
257 Interpretation*, John Wiley & Sons, New York, pp. 756
- 258 12. Lubin, D and R. Massom (eds.), 2006: *Sea ice. In: Polar Remote Sensing, Vol-1-Atmosphere and Oceans*,
259 Springer-Praxis, Germany, pp. 309–609
- 260 13. Piwowar, J.M., and E.F. LeDrew, 1996: Principal components analysis of Arctic ice conditions between 1978
261 and 1987 as observed from the SMMR data record, *Canadian Journal of Remote Sensing*, Vol. 22(4), pp.
262 390–403
- 263 14. Rajak, D.R.; R.K. Kamaljit Singh; P. Jayaprasad; S.R. Oza; R. Sharma and R. Kumar, 2015: Sea ice occurrence
264 probability data and its applications over the Antarctica, *Journal of Geomatics*, Vol. 9(2), pp. 193–197
- 265 15. Remund, Q.P. and D.G. Long, 1999: Sea ice extent mapping using Ku band scatterometer data, *Journal of
266 Geophysical Research*, 104(C5), pp. 11,515–11,527
- 267 16. Remund, Q.P. and D.G. Long, 2014: A decade of QuikSCAT scatterometer sea ice extent data, *IEEE
268 Transactions on geoscience and remote sensing*, 52(7), pp. 4281–4290
- 269 17. Rothrock, D.A. and D.R. Thomas, 1988: Principal component analysis of satellite passive microwave data
270 over sea ice, *Journal of Geophysical Research*, Vol. 93(C3), pp. 2321–2332
- 271 18. SCATSAT1 DP Team, 2017: SCATSAT-1 level 4 data products format document, MDPD/SIPG, Space
272 Applications Centre-ISRO, Ahmedabad, India, SC1/DP/L4FORMAT-DOC/V1.1/JUL2017
- 273 19. Spreen, G., L. Kaleschke, and G. Heygster, 2008: Sea ice remote sensing using AMSR-E 89 GHz channels
274 *Journal of Geophysical Research*, Vol. 113(C02S03).
- 275 20. Timmerman, R., A. Beckmann and H.H. Helmer, 2001: The role of sea ice in the fresh-water budget of the
276 Weddell Sea, Antarctica, *Annals of Glaciology*, 33, pp. 419–424
- 277 21. Tou, J.T., and R.C. Gonzalez, 1974: *Pattern recognition principles*, Addison-Wesley, London
- 278 22. Zwally, H. J., J.C. Comiso, C.L. Parkinson, W.J. Campbell, F.D. Carsey, and P. Gloersen, 1983: Antarctic sea
279 ice 1973 –1976 from satellite passive microwave observations, NASA Special Publication, 459, p. 206.

280 Figures and tables follow.

281



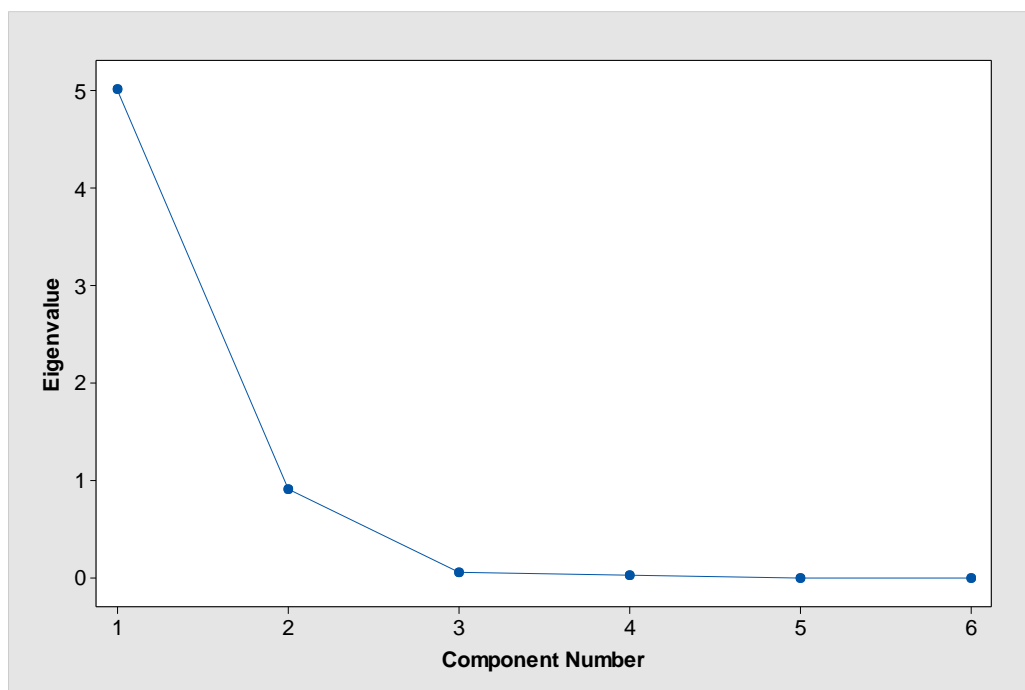
282

283

284

Figure. 1: Location map for the regions (marked in different colours) used in PCA overlaid on SCATSAT-1 backscatter (σ_0) data.

285

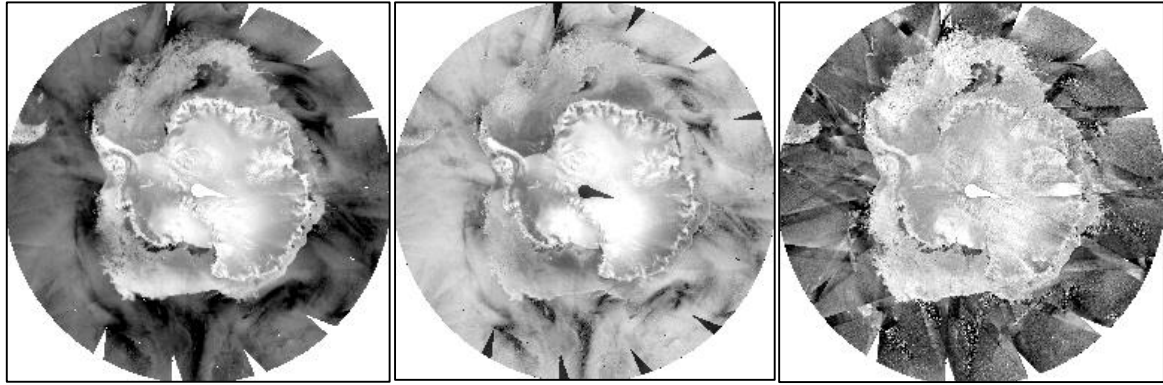


286

287

Figure. 2: Scree plot from the principal component analysis.

288

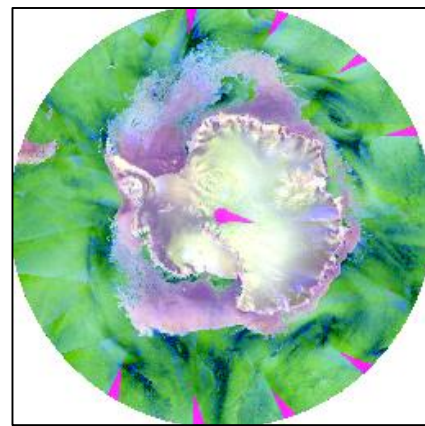


289
290
291

(a)

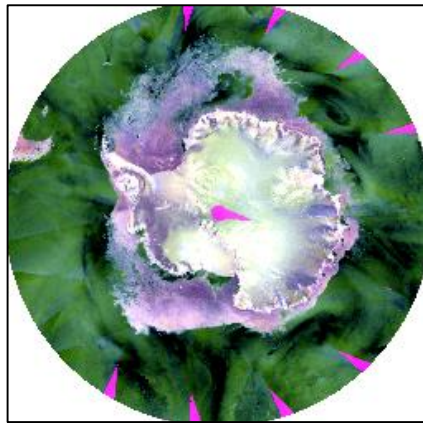
(b)

(c)



292

(d)

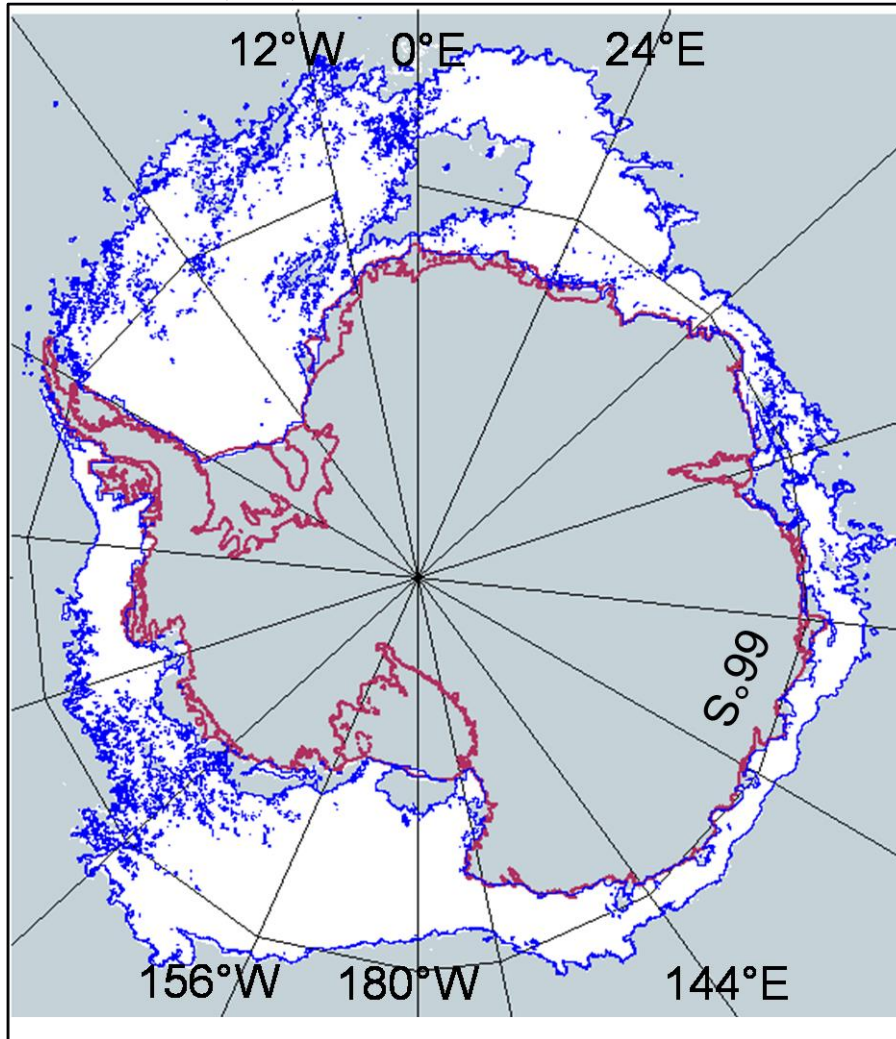


(e)

293
294

295
296
297

Figure. 3: (a) –(c)- First (PC1), Second (PC2) and Third (PC3) Principal Component respectively generated from six scatterometer parameters; (d)- False colour composite prepared using PC1, PC2 and PC3 as red, green and blue channel respectively, and (e) HSV sharpened imaged of (d).



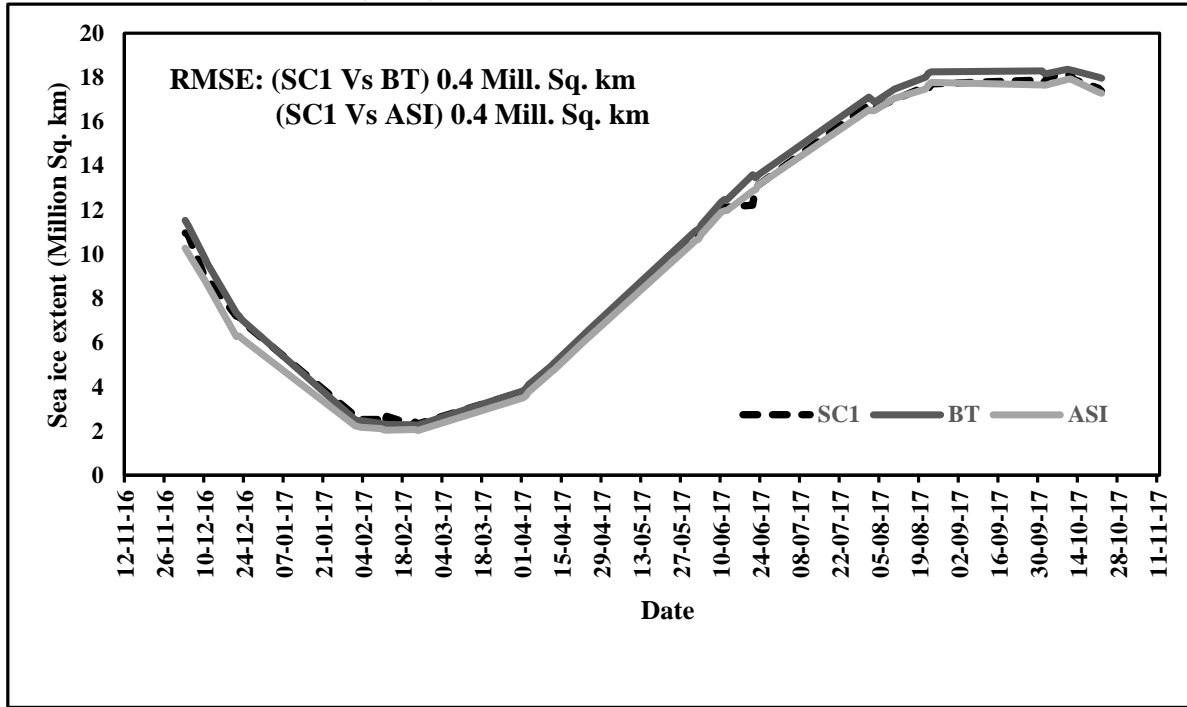
298

299

300

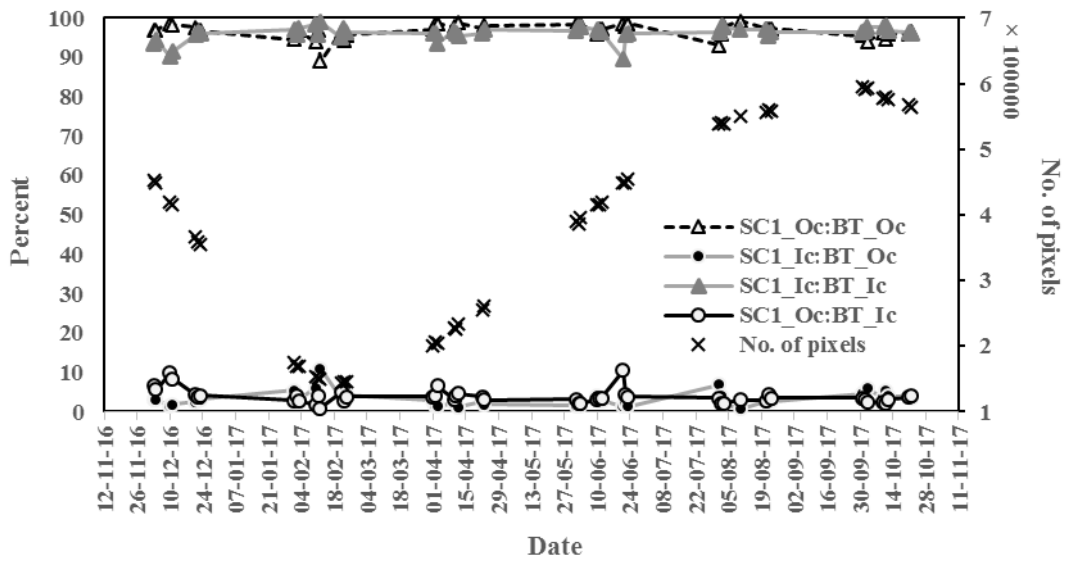
301

Fig. 4: Antarctic sea ice (white shade) extent from SCATSAT-1. Overlaid (blue contour) on the image is the sea ice boundary estimated from passive microwave (PMW) data for the same day (3 December, 2016). The SIE obtained from SCATSAT-1 is $\sim 10.7 \times 10^6 \text{ km}^2$ while that from PMW is $10.3 \times 10^6 \text{ km}^2$.



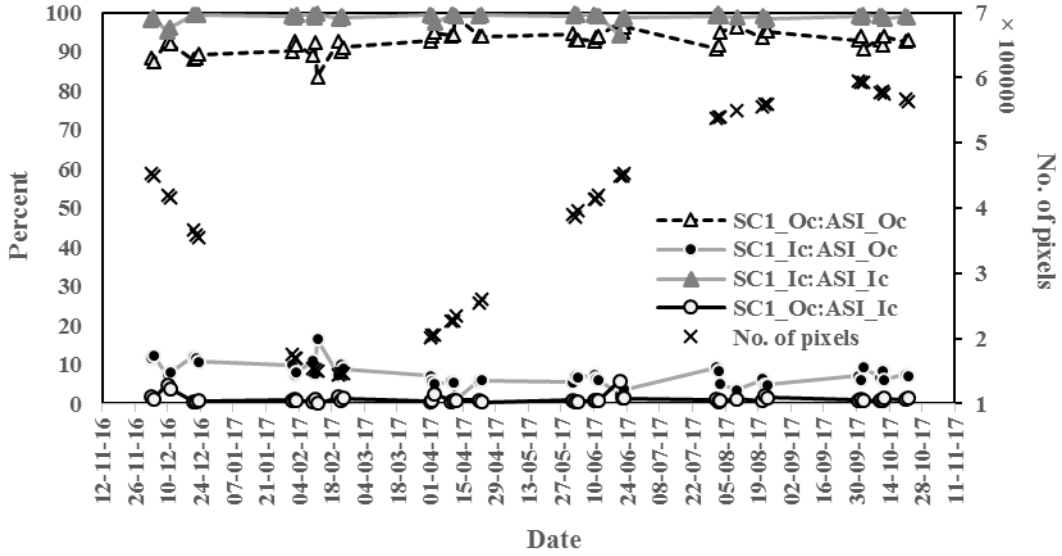
302
 303
 304
 305

Figure. 5: Comparison of sea ice extents for the period December, 2016 to October, 2017 from SCATSAT-1, Bootstrap and ASI algorithms. A correlation coefficient of 0.99 is obtained in both the comparisons viz., SCATSAT-1 Vs BT and SCATSAT-1 Vs ASI.



306
 307

(a).



308

309

(b).

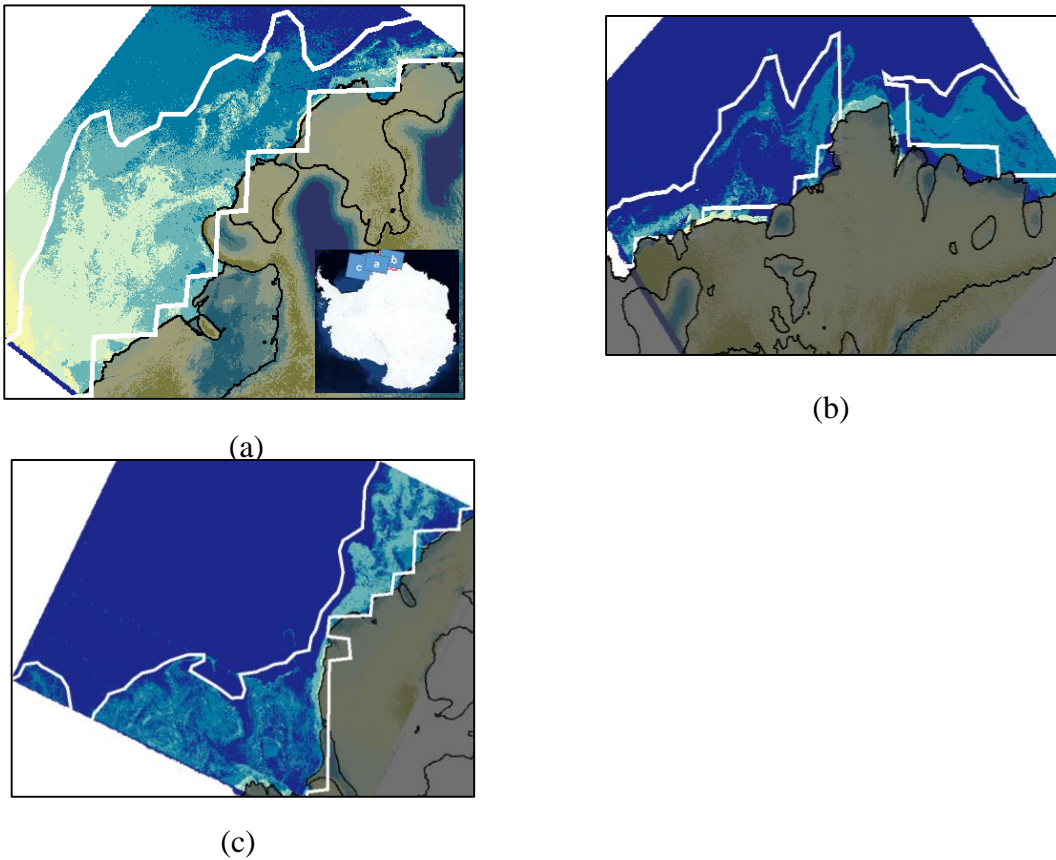
310

311

312

Figure. 6: Pixel-wise mapping accuracy for the comparison between (a) SCATSAT-1 (SC1) and Bootstrap (BT), and (b) SC1 and ASI sea ice extent estimates. 'Oc' represents ocean and 'Ic' represents sea ice. Details are discussed in Section 4.

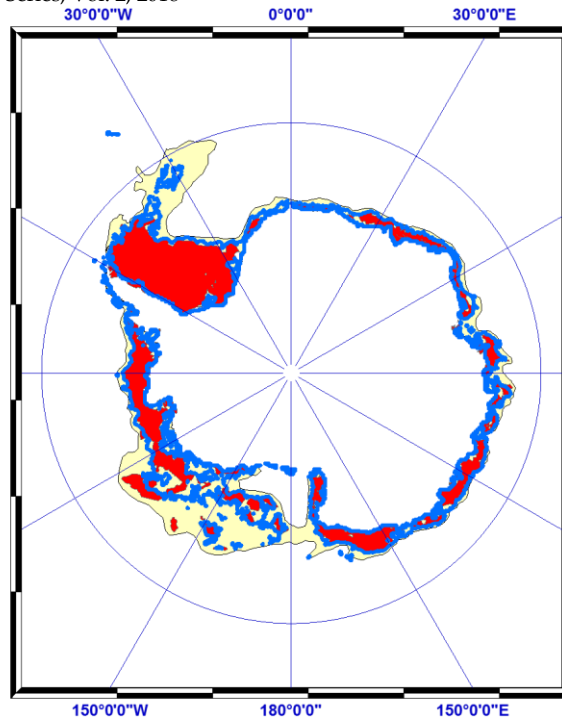
313



314

315

Figure. 7: Comparison with Sentinel-1 SAR data. SCATSAT-1 derived sea ice extent (white contour) is overlaid over SAR imagery. Inset (a) shows the locations of these three imagery.



316

317

318

Figure. 8: Comparison of SCATSAT-1 sea ice edge (blue solid contour) with US NIC ice chart. Yellow regions are the Marginal Ice Zones while red regions are having higher sea ice concentration.

319

320

Table 1: Principal Component coefficients for the 6 parameters used in the study. H and V are horizontal and vertical polarizations; Tb is brightness temperature, Gam is γ_0 and Sig is σ_0 .

321

Coeff ▶ Parameters ▼	Coeff 1	Coeff 2	Coeff 3
Tb_H	0.3623	-0.6015	-0.08589
Tb_V	0.3668	-0.5857	-0.1571
Gam_H	0.4379	0.1604	0.5315
Gam_V	0.4185	0.3493	-0.4514
Sig_H	0.4380	0.1602	0.5303
Sig_V	0.4186	0.3490	-0.4476

322

323

Table 2: F-test statistics for (a) SCATSAT-1 and BT comparison, and (b) SCATSAT-1 and ASI.

324

(a)

	BT	SCI
Mean	10.51	10.25
Variance	37.33	35.09
Observations	48.00	48.00
df	47.00	47.00
F	1.06	
P(F<=f) one-tail	0.42	
F Critical one-tail	1.62	

(b)

	ASI	SCI
Mean	10.00	10.25
Variance	36.32	35.09
Observations	48.00	48.00
df	47.00	47.00
F	1.03	
P(F<=f) one-tail	0.45	
F Critical one-tail	1.62	

325

326
 327

Table 3: Student's t-test results for (a) SCATSAT-1(SC1) Versus Bootstrap (BT) and (b) SC1 Versus ASI.

	<i>BT</i>	<i>SCI</i>
Mean	10.51	10.25
Variance	37.33	35.09
Observations	48.00	48.00
Pooled Variance	36.21	
Hypothesized Mean Difference	0.00	
df	94.00	
t Stat	0.21	
P(T<=t) two-tail	0.83	
t Critical two-tail	1.99	

328
 329

(a)

	<i>ASI</i>	<i>SCI</i>
Mean	10.00	10.25
Variance	36.32	35.09
Observations	48.00	48.00
Pooled Variance	35.71	
Hypothesized Mean Difference	0.00	
df	94.00	
t Stat	-0.20	
P(T<=t) two-tail	0.84	
t Critical two-tail	1.99	

330
 331

(b)